Journal of Materials Science & Technology 240 (2026) 27–34

Contents lists available at ScienceDirect

Journal of Materials Science & Technology

journal homepage: www.elsevier.com/locate/jmst

Research Article

Insights into crystal growth and morphology evolution mechanism of multi-component carbide: Experiments and first-principles calculations

Yong Fan[a], Yuyao Chen[a], Jin Wang[a], Lei Gu[a], Kaixuan Zhou[a], Yuanyuan Gong[b], Wei Liu[a,c,*], Yonghao Zhao[a,d,*], Xiangfa Liu[e], Jinfeng Nie[a,*]

[a] Nano and Heterogeneous Materials Center, School of Materials Science and Engineering, Nanjing University of Science and Technology, Nanjing 210094, China
[b] MIIT Key Laboratory of Advanced Metallic and Intermetallic Materials Technology, School of Materials Science and Engineering, Nanjing University of Science and Technology, Nanjing 210094, China
[c] State Key Laboratory of Rare Earth Resource Utilization, Changchun Institute of Applied Chemistry, Chinese Academy of Sciences, Changchun 130022, China
[d] School of Materials Science and Engineering, Hohai University, Changzhou 213200, China
[e] Key Laboratory for Liquid-Solid Structural Evolution and Processing of Materials, Ministry of Education, Shandong University, Jinan 250061, China

ARTICLE INFO

Article history:
Received 16 December 2024
Revised 17 February 2025
Accepted 12 March 2025
Available online 30 April 2025

Keywords:
Multi-component carbide
First-principles calculations
Crystal growth
Morphology evolution mechanism

ABSTRACT

Multi-component transition metal carbides (MTMCs) have garnered significant attention for their outstanding high-temperature stability and versatile properties, which make them ideal candidates for a wide range of industrial applications. However, the underlying mechanisms governing the crystal growth and morphological evolution of MTMCs remain poorly understood, hindering the design of materials with tailored characteristics. In this paper, we employ an in-situ liquid-solid reaction method to synthesize (HfTaZrNbTi)C MTMC powders and explore their crystal growth and morphology evolution. The synthesized (TiZrHfNbTa)C powders exhibit two distinct morphologies: cubic, primarily composed of Ti, Hf, Ta, and Zr with a small amount of Nb, and octahedral, rich in Ti and Ta with minor amounts of Hf, Nb, and Zr. First-principles calculations show that the surface energy of the (100) plane is lower than the (111) plane, leading to the formation of the cubic morphology. The octahedral morphology forms due to decreased mixing entropy and higher theoretical density compared to cubic particles. Our findings provide valuable insights into the crystal growth and morphology evolution mechanisms of high-entropy ceramics, contributing to the rational design of MTMCs with engineered crystal structures for diverse structural and functional applications.

1. Introduction

Transition metal carbides (TMCs), such as TaC, ZrC, and TiC, have attracted considerable research interest due to their high hardness, superior thermal stability, and excellent corrosion resistance [1–3]. These TMCs belong to the ultra-high-temperature ceramics (UHTCs) family and have great potential applications in structural components and thermal protection systems [4–6]. However, due to the inherent limitations in performance improvement and the increasing demands of modern industrial developments, TMCs are gradually becoming inadequate to meet the requirements of advanced applications.

Over the past decade, the design concept of multi-component solid solutions, also commonly referred to as medium- or high-entropy, has proven to be a highly promising strategy for enhancing the comprehensive properties of UHTCs [7–11]. The synthesized multi-component transition metal carbides (MTMCs) exhibit superior structural stability and corrosion resistance compared to single-component TMCs, particularly in extreme environments such as high-pressure, high-temperature oxidation, and high-speed airflow [12–14]. The first-principles calculations have also been used to explore the phase stability and mechanical properties of MTMCs, providing essential insights into their thermodynamic behavior and further reinforcing the potential of these materials for UHTC applications [15,16].

* Corresponding authors.
E-mail addresses: weiliu@ciac.ac.cn (W. Liu), yhzhao@njust.edu.cn (Y. Zhao), niejinfeng@njust.edu.cn (J. Nie).

https://doi.org/10.1016/j.jmst.2025.03.057
1005-0302/

Inspired by the excellent performance of MTMCs, a number of MTMCs have been successfully prepared and some exciting results have been obtained, greatly expanding the application boundaries of UHTCs [17–19]. Notably, the preparation of MTMC powders is a crucial prerequisite for the synthesis of ceramic materials. To date, a variety of solid-state reaction methods, including solid-state sintering [20], carbothermal reaction [21–23], and magnesiothermic reduction [24], have been proposed for the synthesis of MTMC powders. For example, Feng et al. [23] synthesized (HfZrTiTaNb)C powders using a two-step method of carbothermal reduction combined with solid solution formation, where the carbothermal reduction was completed after heating to 1600 °C, followed by solid solution formation at 2000 °C. Ye et al. [22] prepared $(Zr_{0.25}Ta_{0.25}Nb_{0.25}Ti_{0.25})C$ powders with particle sizes of 0.5–2 μm using a one-step carbothermal reduction method at 2200 °C.

Despite the products of the solid-state reaction method possessing excellent compositional uniformity, it still suffers from significant drawbacks such as a complex preparation process, high energy consumption, and lengthy preparation times. Therefore, the rapid advancement and widespread application of MTMC materials have been hindered. Several innovative techniques have been proposed for the synthesis of MTMC powders, including the polymer-derived ceramic route [25], molten salt synthesis [26], and liquid precursor method [27]. Although these techniques offer benefits like low reaction temperatures and nanoscale powder sizes, they still face unresolved challenges such as the high cost of metal powders and the use of toxic inorganic reactants. Consequently, there is a critical need for a low-cost, energy-efficient, and highly effective method to synthesize MTMC powders.

Furthermore, although some studies on the crystal growth and morphology evolution of transition metal carbides have been reported [28,29], there are few relevant studies on MTMCs. From the perspective of crystal growth, the crystalline morphology and exposed facets of the powder have a strong influence on the physical and chemical properties of the material. By designing and controlling the special preferred orientation exposure surface, further engineering and functional performance can be obtained such as electromagnetic interference shielding, mechanical properties, and catalysis [30,31]. In addition to the limited research on the crystal growth process of MTMCs, more importantly, the fundamental understanding of the relationship between the crystalline morphology of the MTMC phase and its constituent element remains a challenge in this field.

In this work, (TiZrHfNbTa)C MTMC powders were synthesized by a novel and efficient in-situ liquid-solid reaction method via a molten aluminum medium. The microstructure, elemental distribution, and three-dimensional morphology of the (TiZrHfNbTa)C MTMC powders were investigated. The structural stability and surface energy of (TiZrHfNbTa)C were calculated by first-principles calculations. By combining experimental results with theoretical calculations, the morphology evolution mechanism of MTMCs was analyzed based on the crystal nucleation and growth theory. These findings significantly contribute to the fundamental understanding of the crystal growth and morphological evolution of MTMCs, which can be of great practical importance for the design of MTMC powders with desired shapes and performance.

2. Materials and methods

The (TiZrHfTaNb)C particles were synthesized via the in-situ liquid-solid reaction method facilitated by the molten aluminum medium. Firstly, the Al-33.3Ni-5.42(TiZrHfTaNb)C (hereafter referred to as Al-Ni-MTMC) alloy ingot containing (TiZrHfTaNb)C particles was prepared by vacuum arc melting method. The nominal composition of the prepared Al-Ni-MTMC master ingot is shown in Table S1 in the Supplementary Materials. The (TiZrHfTaNb)C particles were then extracted from the obtained aluminum matrix composite ingot using a 25 vol% HCl solution. The detailed experimental procedures, characterization methods, and the first-principles calculations are also provided in the Supplementary Materials. Specially, the constructed crystal structures of the (TiZrHfNbTa)C system, along with the corresponding fitted energy-volume curves, are presented in Figs. S1 and S2 in the Supplementary Information, respectively. Furthermore, Fig. S3 systematically illustrates the surface configurations of (100), TM-(111), and C-(111) surfaces of the MTMC.

3. Results and discussion

Fig. 1(a) shows the X-ray diffraction (XRD) pattern of the (TiZrHfTaNb)C particles extracted from the as-cast Al-Ni-MTMC alloy. The diffraction peaks correspond to the (TiZrHfNbTa)C carbide phase with a face-centered cubic (FCC) rock-salt structure, as well as the Al_3Ni_2 intermetallic compound. Meanwhile, it is noticed that there are two distinct peaks within the carbide peaks, indicating the presence of two different types of carbide compositions. Fig. 1(b) shows a typical scanning electron microscope (SEM) morphology of the synthesized carbide particles. The synthesized carbides exhibit two distinct morphologies: one exhibits a cubic morphology enclosed by {100} planes, as shown in the red rectangle, and the other is an octahedral morphology enclosed by {111} planes, as shown in the blue rectangle. To further investigate the elemental composition of these two types of carbides, electron probe microanalysis (EPMA) was conducted. The EPMA mapping analysis for the cubic and octahedral morphologies is presented in Fig. 1(c, d), respectively. Fig. 1(c) indicates that the cubic particle (TiZrHfNbTa)C is mainly composed of Ti, Hf, Ta, Zr, and C, with a small amount of Nb, and barely contains Ni and Al. The octahedron particle (Fig. 1(d)) is rich in Ti, Ta, and C, with a small amount of Hf, Nb. and Zr, and barely contains Ni and Al.

Both the XRD and EPMA analyses confirmed that the (TiZrHfNbTa)C MTMC with two typical crystal morphologies was successfully synthesized using the in-situ liquid-solid reaction method. During the in-situ reaction, as the temperature increases, the dissolved C atoms react with the dissolved Hf, Ta, Zr, Nb, and Ti in the melt, forming (TiZrHfNbTa)C MTMC. Different crystal morphologies could be related to the distinct growth mechanisms in the complex melt environment. Besides, the MTMC powders barely contain Ni atoms although Ni-C alloy was used as a carbon source in the preparation of MTMC. Fig. S1 proves that Ni atoms are difficult to enter the MTMC structure and exist as a Ni-Al intermetallic compound through first principles calculation.

A representative cubic (TiZrHfTaNb)C particle with a particle size of 2 μm was selected and was further investigated the nano-level crystal structure information and element distribution by transmission electron microscopy (TEM) analysis. The TEM specimen was prepared using a Focused Ion Beam (FIB) system as shown in Fig. S2. Fig. 2(a) shows a high-angle annular dark field (HAADF) image of the MTMC particle, exhibiting a cubic shape with distinct regions of contrast change at the edges. The corresponding energy dispersive spectrometer (EDS) mapping of this particle (labeled by a red rectangle in Fig. 2(a)) is depicted in Fig. 2(a1). An obvious $Nb_{rich}C$ region is observed at the edge of the particle. The quantitative EDS line-scan data, presented in Fig. S3, shows a significant increase in the atomic fraction of Nb from the core to the outer shell, confirming the formation of a $Nb_{rich}C$ shell. Specifically, the Nb content in the shell region reaches approximately 50 at.%–60 at.% in the outermost layer, while the core region contains much lower Nb concentrations, remaining below 20 at.%. This distinct difference in Nb concentration defines the boundary between the core and the shell. The line-scan data also indicate that this increase in Nb concentration occurs at approxi-

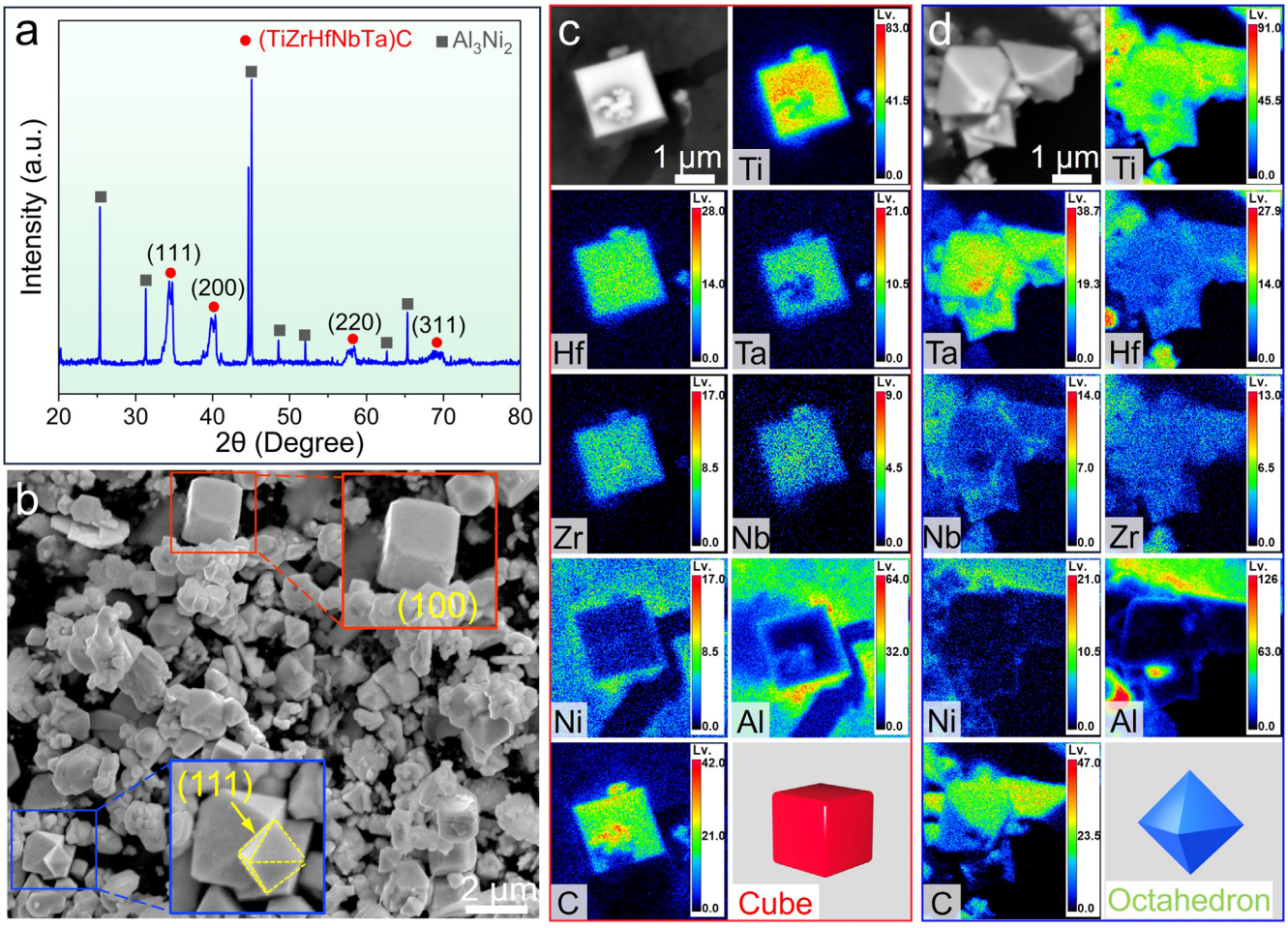

Fig. 1. (a) XRD patterns of powders extracted from the as-cast Al-Ni-MTMC alloy; (b) the typical SEM image of the extracted (TiZrHfTaNb)C particles; (c, d) the typical SEM images, EPMA mappings and schematic models of the cube and octahedron particles, respectively.

mately 150 nm from the particle center, clearly marking the transition between the $(TiZrHfTa)_{rich}C$ core and the $Nb_{rich}C$ shell. The core, primarily composed of Ti, Zr, Hf, and Ta, exhibits a uniform distribution of these elements, with their concentrations remaining stable throughout the core region and only decreasing as they approach the shell. The high-resolution TEM (HRTEM) images are shown in Fig. 2(b, d). Fig. 2(c) gives the Fast Fourier transform (FFT) patterns of the corresponding HRTEM images along the [001] zone axis, confirming the FCC metal carbides crystal structure. Fig. 2(d) exhibits the atomic arrangements on the {0011} plane of the (TiZrHfTaNb)C. The measured interplanar spacing of the $(\bar{2}00)$ crystal plane of (TiZrHfTaNb)C is 0.241 nm according to Fig. 2(e). The schematic atomic model of the MTMC with the FCC crystal structure is shown in Fig. 2(f), which is viewed from the $[100]_{MTMC}$. The atomic arrangement in the {100} planes is neatly arranged, and it is consistent with the crystal structure shown in Fig. 2(g) presents a schematic diagram of the core-shell structured cubic (TiZrHfTaNb)C particle, with a $(TiZrHfTa)_{rich}C$ core and a $Nb_{rich}C$ shell, consistent with the elemental distribution data.

The first-principles calculations were performed to study the formation mechanism of the $Nb_{rich}C$ shell existing in the cubic (TiZrHfTaNb)C particle on the (001) surface. The surface models of MTMC were constructed as shown in Fig. 2(h) to analyze the energy changes during the formation of the $Nb_{rich}C$ shell layer. For Model-0, the atoms in the (001) plane are composed of Ti, Zr, Hf, and Ta elements, and the Nb atoms involved are all located at the second layer. The surface models were reconstructed via interdiffusion between the terminating Ti, Zr, Hf, and Ta atoms and the subsurface surface Nb atoms. As a result, the surface models shown in Fig. 2(h) were formed, named Model-*i*, $i = 1$ to 4. For Model-4, the atoms on the surface are all Nb atoms, while the atoms randomly distributed in the bulk are all Ti, Zr, Hf, and Ta atoms. Fig. 2(i) shows the energy change ΔE_i^{sur} due to surface atomic reconstruction, expressed as follows:

$$\Delta E_i^{sur} = E_i^{sur} - E_0^{sur} \quad (1)$$

where $E_i^{sur}$and E_0^{sur} are the total ground state energies of model-*i* and model-0, respectively. The result shows that the ΔE_i^{sur} decreases first and then increases, but is always less than zero during the continuous mutual diffusion process between Nb and other metal atoms. This indicates that Nb elements tend to diffuse to the terminal position of the (001) surface of the shell. The calculation results confirm that the initial Nb element in the subsurface (001) surface is in an unbalanced state and tends to evolve into a surface model with a $Nb_{rich}C$ shell. In Model-2, half of the Nb atoms have diffused to the outermost surface, while the remaining Nb atoms reside in the subsurface layer, leading to the lowest energy change and the highest thermodynamic stability for this model. It should be noted that kinetic effects, such as diffusion, are not taken into consideration in the above ab initio calculations. Therefore, a NbC shell, rather than the $Nb_{rich}C$ shell observed in experiments, is predicted. However, these ab initio calculation results are still effective in explaining the formation mechanism of the $Nb_{rich}C$ shell at the surface of the carbide structure [32].

A representative truncated octahedral (TiZrHfTaNb)C particle was then selected and characterized the structure and element dis-

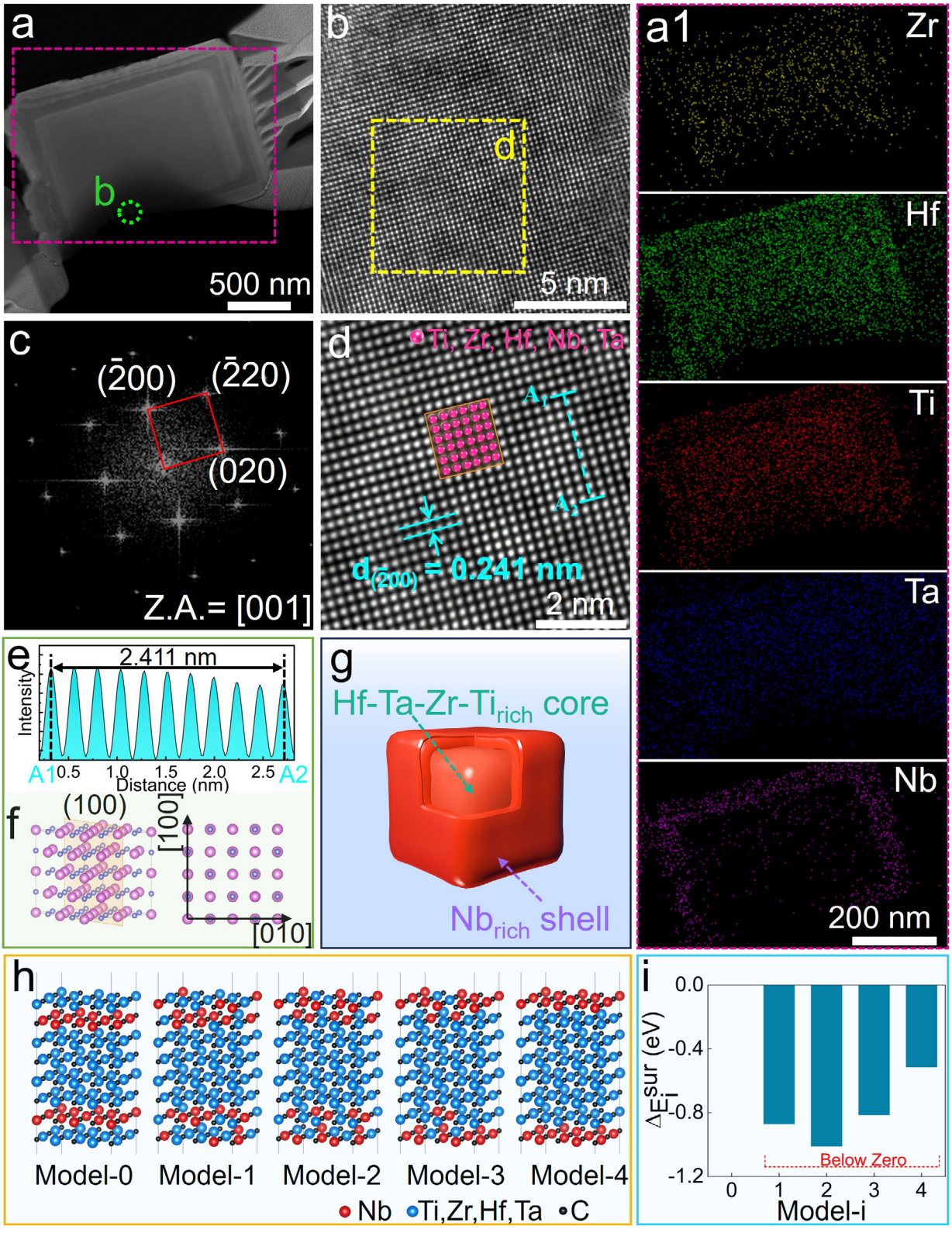

Fig. 2. The HRTEM analysis of the cubic MTMC particle; (a) The HAADF image; (a1) the corresponding EDS maps; (b) the HRTEM graph; (c) the corresponding FFT pattern; (d) HRTEM image showing the atomic structure; (e) the intensity of the arrows from A1 to A2 in (d); (f) schematic illustration of the atomic structure and atomic configurations on the {001} plane, the large pink spheres represent the Ti, Zr, Hf, Nb and Ta atoms, and the small black spheres represent the C atoms; (g) schematic drawing of the core-shell structure. (h) surface model-0 to surface model-4; (i) energy change ΔE_i^{sur} induced by the (100) MTMC surface reconstruction.

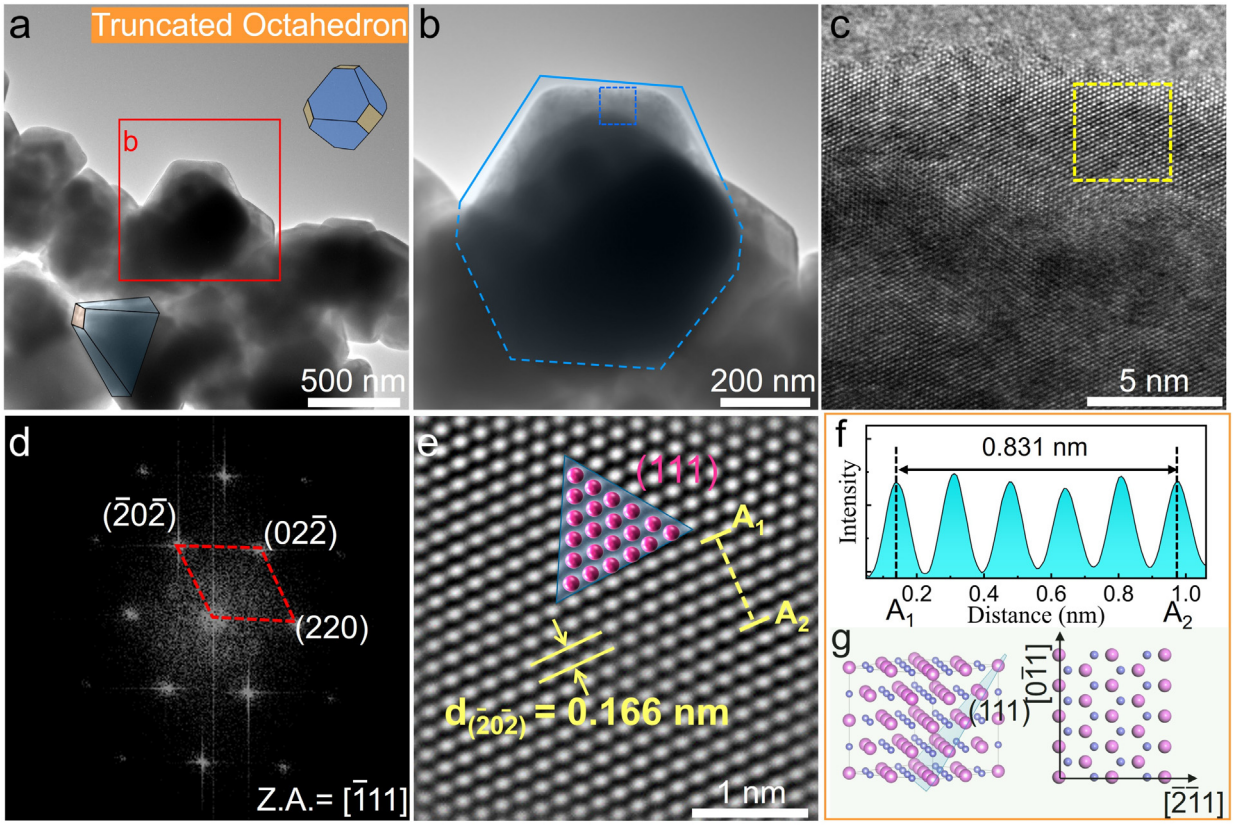

Fig. 3. The HRTEM analysis of the truncated octahedron MTMC particle; (a) HAADF image; (b) high-magnification of (a); (c) HRTEM graph; (d) the corresponding FFT pattern; (e) HRTEM image showing the atomic structure; (f) the intensity of the arrows from A1 to A2 in (e); (g) schematic illustration of the atomic structure and atomic configurations on the {111} plane.

tribution in detail. Fig. 3(a, b) shows the typical HAADF images of the (TiZrHfTaNb)C particles with truncated octahedral morphology. In addition, the EDS mapping of these particles is depicted in Fig. S4. The results show that Hf, Ta, Zr, Nb, and Ti elements are uniformly distributed at the micrometer scale without obvious element segregation for truncated octahedral (TiZrHfTaNb)C particle. The corresponding HRTEM image (Fig. 3(c)) indicates that the particle exhibits a regular lattice structure. Fig. 3(d) gives the Fast Fourier transform (FFT) patterns of the corresponding HRTEM images along the [111] zone axis. Fig. 3(e) exhibits the atomic arrangement on the {111} plane of the (TiZrHfTaNb)C. The measured interplanar spacing of the $(20\bar{2})$ crystal plane of (TiZrHfTaNb)C is 0.166 nm according to Fig. 3(f). Fig. 3(g) offers a schematic representation of the atomic arrangement of the (TiZrHfTaNb)C crystal along the {111} planes, which is consistent with the crystal structure shown in Fig. 3(e).

Based on the above experimental results, the (TiZrHfTaNb)C powders with two different morphologies were successfully synthesized using the in-situ liquid-solid reaction method. In general, the ultimate crystal morphology is primarily determined by two key factors: the intrinsic crystal structure and the external conditions present during its growth. According to Wulff's theorem, the equilibrium crystal morphology is the shape with the lowest total surface energy, so the crystal planes with lower surface energy characterized by high reticular densities and large interplanar spacings will eventually be exposed [33]. Generally, for FCC structure, (100) and (111) planes are the most typically close-packed with lower surface energies, thus eventually becoming stable exposed crystal surfaces [34,35]. The surface energy (γ_{surf}) of (TiZrHfTaNb)C (100) and (111) surfaces was calculated using the first principles method and the calculation procedure is given in detail in the Supplementary Materials. Fig. 4(a, b) illustrates the critical nucleation and growth morphology for FCC structure particles as a function of the (001) and (111) surface energy ratio R ($\gamma 100/\gamma 111$) based on the Wulff construction [36]. The relationship between the value of R and the equilibrium morphology is described in the Supplementary Materials. Fig. 4(c) plots the surface energy calculation results of (TiZrHfTaNb)C (100) and (111) surfaces. Generally, lower surface energy indicates higher surface stability and slower crystallization rate along the direction normal to the surface [37]. The results show that the surface energy of (100) surface is always lower than TM-terminated and C-terminated MTMC (111) surfaces. Therefore, the most stable surface of MTMC is the (100) plane, which is more likely to be the exposed crystal plane. Fig. 4(d) gives the calculated surface energy ratio R with respect to the chemical potential of the carbon atoms ($\Delta\mu_C$). The R value ranges from $0.23 < R < 0.26$ to $0.52 < R < 0.68$, suggesting that the MTMC tends to form a cube and truncated cube morphologies, while the ideal octahedra morphology is difficult to form in the melt theoretically. In general, the final morphology of the actual crystal depends on a combination of its intrinsic lattice structure and the external growth environment. The intrinsic crystal structure leads to the formation of an equilibrium morphology with the lowest surface energy. However, the varied external environmental factors, such as complicated melt environments and mass transport processes of the reactants, cause the crystals to deviate from the equilibrium morphology by changing the growth velocity in other directions [38,39].

Based on the previous analysis of SEM, EDS, and first-principles calculations, a schematic illustration of the reaction and morphology evolution of MTMC particles in the Al melt was proposed, as shown in Fig. 5. In this study, the system consists of five transi-

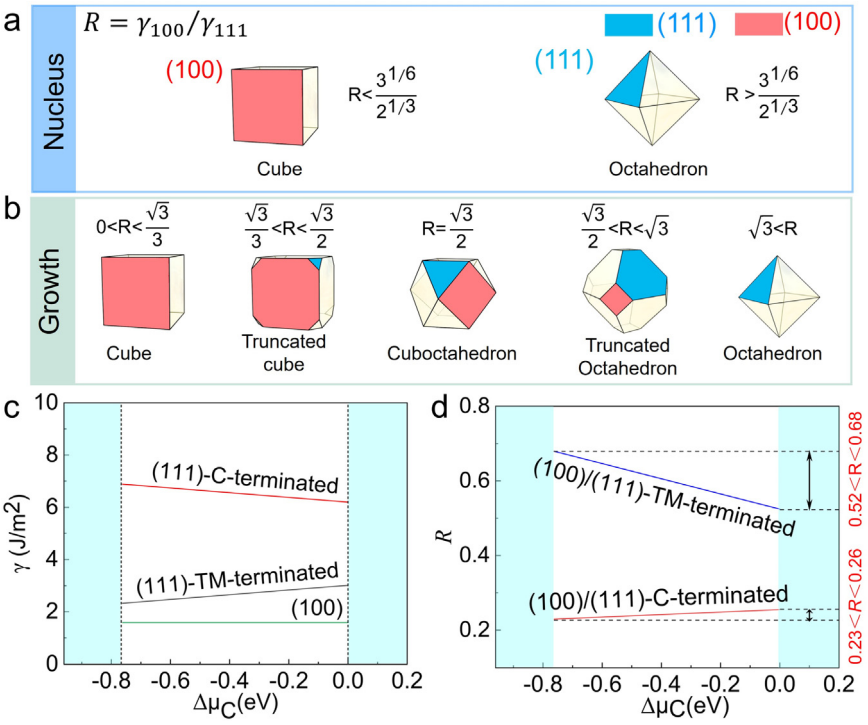

Fig. 4. (a, b) Schematic illustrations of the morphology of nucleus and growth, as a function of the (100) and (111) surface energy ratio R ($\gamma 100/\gamma 111$), respectively. (Notes: $\frac{3^{1/6}}{2^{1/3}} \approx 0.95$, $\frac{\sqrt{3}}{3} \approx 0.58$, $\frac{\sqrt{3}}{2} \approx 0.87$, $\sqrt{3} \approx 1.73$); (c) surface energy of the (100) and (111) slabs of the (TiZrHfNbTa)C as a function of the C atom chemical potential; (d) surface energy ratio R value as a function of the C atom chemical potential.

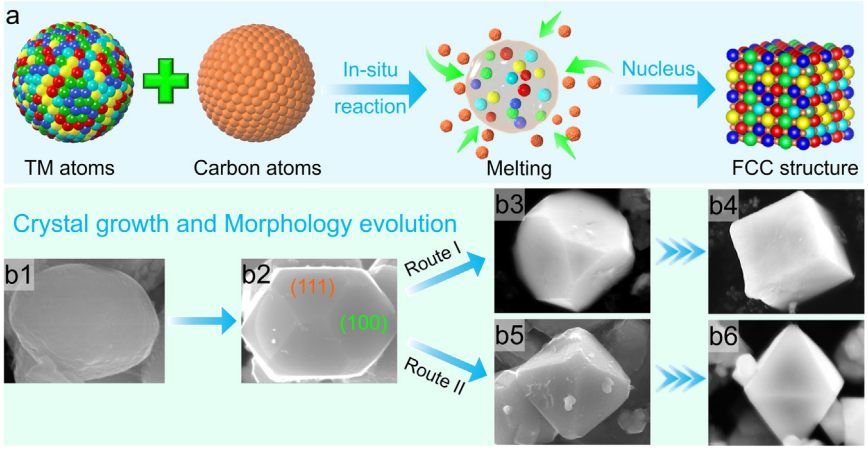

Fig. 5. Schematic diagram of the crystal growth and morphology evolution process of the MTMC; (a) the process of the reaction and nucleation; (b1–b6) the process of the growth and typical SEM images.

tion metals and carbon atoms, as shown in Fig. 5(a). During the in-situ reaction, as the temperature increases, the dissolved transition metals Hf, Ta, Zr, Nb, and Ti ([Me]) react with the dissolved C atoms ([C]) in the Al molten to form MTMC nuclei by the following reaction (1):

$$[Me]+[C]= MTMC \quad (2)$$

Table S3 lists the mixing enthalpy (ΔH_{mix}) of transition metals and carbon elements. It can be found that the ΔH_{mix} of transition group metals and C elements is in the order of Zr > Hf > Ti > Nb> Ta [40]. This indicates that the interaction between carbon and Group IV elements (Ti, Zr, Hf) is stronger compared to that with Group V elements (Nb, Ta).

It is important to note that kinetic effects, such as diffusivity, are also critical factors in understanding the reaction sequence of transition metal atoms in the Al melt. The diffusivity D^i of an element i diffusing in Al matrix is given by the relation [41]:

$$D^i = D_0^i \exp\left(-\frac{Q^i}{RT}\right) \quad (3)$$

where Q^i is denoted as activation energy and D_0^i as the pre-exponential factor. T denotes the absolute temperature and R denotes the gas constant.

Based on theoretical calculations by Luo et al. [42] and experimental values by Knipling et al. [43], the diffusivity of Group IV elements in Al follows the order: $D^{Ti} > D^{Zr} > D^{Hf}$. Additionally, the diffusivity of Group V elements, Ta and Nb, are significantly lower

than those of Group IV elements (Ti, Zr, Hf) due to strong solute-vacancy repulsion [43]. This slower diffusivity of Ta and Nb means they are less likely to rapidly participate in carbide formation during the initial stages of the reaction. Furthermore, it should be noted that the density of Ta (16.65 g/cm^3) is significantly higher than that of the other atoms. Consequently, the diffusivity order of elements in the Al melt is $D^{Zr} > D^{Ti} > D^{Hf} \gg D^{Nb} > D^{Ta}$.

The transition metals were added in a specific order based on their melting points. As Ta has the highest melting point, it was positioned furthest from the Ni-C alloy. As the arc melting process rapidly exceeded 2000 °C, Al melted in a short time, and the in-situ liquid-solid reaction between the transition metals and carbon atoms occurred rapidly. During the melt-flowing process, the more reactive and diffusible elements (Ti, Zr, Hf) spontaneously diffuse towards the surface of the melt and adsorb onto the C atoms. This results in higher concentrations of these elements at the contact interface, facilitating the rapid reaction between dissolved carbon atoms and transition metal atoms, leading to the formation of a ZrC+HfC+TiC-based solid solution. On the other hand, Ta, with its slower diffusion rate, participates in carbide formation at a later stage of the reaction.

Generally, when an element with a larger lattice constant enters a host with a smaller lattice constant, significant lattice distortion occurs, increasing local strain energy and making diffusion less thermodynamically favorable. Gautam et al. [44] calculated the lattice constants of TaC and NbC as 4.44 Å and 4.47 Å, respectively. Extensive theoretical and experimental results further confirm that NbC consistently exhibits a larger lattice constant than TaC [45–47]. Therefore, TaC is more likely to diffuse into the ZrC+HfC+TiC-based solid solution compared to NbC, leading to the formation of particles primarily composed of Ti, Hf, Ta, and Zr. Due to the highest mixing enthalpy with carbon and the slowest diffusion rate in Al, the remaining C atoms predominantly react with unreacted Ta atoms to form TaC-based solid solution structures. Furthermore, TiC, having the lowest lattice constant and the fastest diffusion rate among the five single-component carbides, exhibits the lowest lattice strain when entering the TaC-based solid solution structure, resulting in carbide particles enriched in Ti and Ta. Thus, due to both thermodynamic and kinetic factors, two types of carbides are formed. The first is primarily composed of Ti, Hf, Ta, and Zr, with a small amount of Nb, and the second is rich in Ti and Ta, with smaller amounts of Hf, Nb, and Zr.

The morphology evolution of cubic and octahedral particles is shown in Fig. 5(b1-b6). After the reaction is complete, during the early growth stage, the carbides exhibit rapid, isotropic growth characteristics, forming near-spherical shapes, as shown in Fig. 5(b1). As the crystal continues to grow, anisotropic features begin to emerge, driven by the reduction in free energy. The spherical crystal becomes unstable, and the facets with lower surface energy, such as (111) and (100) planes gradually appear. Eventually, the crystal adopts a cubic morphology, surrounded by six (100) planes and eight (111) planes, resulting in a cuboctahedral shape, as shown in Fig. 5(b2).

For the particles that are primarily composed of Ti, Hf, Ta, Zr, and a small amount of Nb, the growth follows Route I. Previous calculations indicate that the (100) surface always exhibits the lowest surface energy compared to both TM-terminated and C-terminated MTMC (111) surfaces. Therefore, the most stable surface of MTMC particles is the (100) facet. This leads to a gradual increase in the area of the (100) surface, while the area of the (111) surface decreases over time, as shown in Fig. 5(b2, b3). Eventually, a cubic crystal morphology surrounded by six (100) planes is formed, as shown in Fig. 5(b4). A notable feature is the presence of a $Nb_{rich}C$ shell on the (100) surface of the cubic MTMC particles, which is driven by surface energy reduction.

As the reaction progresses, the remaining carbon atoms primarily react with Ta at the later stages of the reaction, forming a TaC-based solid solution structure. Subsequently, Ti enters the TaC-based solid solution, forming carbides mainly composed of Ta and Ti. At this stage, the local chemical potential of carbon decreases. It leads to a reduction in the surface energy of the (111) plane of the TaC-based solid solution. The surface energy of the (111) plane becomes lower than that of the (100) plane and more similar to the pure metal Ta(111) surface [48,49]. This reduction in surface energy stabilizes the (111) plane in the final crystal structure, rather than being replaced by the (100) planes. It is essential to note that the lower high-temperature stability of octahedral particles compared to cubic particles leads to decreased mixing entropy [50]. Furthermore, the movement and transmission of atoms with high density require more energy, and the deposition of atoms on the most close-packed plane (111) may be reduced which finally changes the growth and the surface energy [39]. As a result, for the particles that are primarily composed of Ti and Ta, the growth follows Route II. The area of the (111) planes is enlarged as shown in Fig. 5(b5), and the ideal octahedral shape is formed as shown in Fig. 5(b6).

4. Conclusions

In conclusion, the (TiZrHfNbTa)C MTMC powders were fabricated via the in-situ liquid-solid reaction method. The crystal growth and morphology evolution mechanisms were investigated based on the experiments and first-principles calculations. The synthesized powders exhibit two typical morphologies, a cubic morphology which is mainly composed of Ti, Hf, Ta, and Zr, with a small amount of Nb, and an octahedral morphology which is rich in Ti, Ta, with a small amount of Hf, Nb and Zr. As for the cubic MTMC particles, the surface energy of the (100) surface is always lower than the (111) surface and the (100) facet tends to be the exposed crystal plane. For particles composed mainly of Ti and Ta metal atoms, the formation of octahedral morphology is primarily driven by the reduction in the surface energy of the (111) plane due to the decreased chemical potential of carbon, which stabilizes the octahedral shape. Additionally, the high theoretical density of octahedral particles and the decreased mixing entropy further contribute to the formation of the octahedral morphology. This work not only provides a new perspective to reveal the growth mechanism of multi-component transition metal carbide particles but also serves as a valuable reference for the design of carbides with desired morphology and superior properties.

Declaration of competing interest

The authors declare that they have no known competing financial interests or personal relationships that could have appeared to influence the work reported in this paper.

CRediT authorship contribution statement

Yong Fan: Methodology, Investigation, Data curation, Writing – original draft, Writing – review & editing. **Yuyao Chen:** Methodology, Data curation, Investigation. **Jin Wang:** Data curation, Investigation. **Lei Gu:** Methodology, Data curation. **Kaixuan Zhou:** Data curation. **Yuanyuan Gong:** Methodology. **Wei Liu:** Methodology, Conceptualization, Supervision. **Yonghao Zhao:** Writing – review & editing. **Xiangfa Liu:** Methodology, Supervision. **Jinfeng Nie:** Conceptualization, Methodology, Writing – review & editing, Funding acquisition. All authors have read the manuscript and agreed to the publication.

Acknowledgements

This work was supported by the National Natural Science Foundation of China (Nos. U24A2026 and 52271033) and the Natural Science Foundation of Jiangsu Province, China (No. BK20221493).

Supplementary materials

Supplementary material associated with this article can be found, in the online version, at doi:10.1016/j.jmst.2025.03.057.

References

[1] D.W. Ni, Y. Cheng, J.P. Zhang, J.X. Liu, J. Zou, B.W. Chen, H.Y. Wu, H.J. Li, S.M. Dong, J.C. Han, X.H. Zhang, Q.G. Fu, G.J. Zhang, J. Adv. Ceram. 11 (2021) 1–56.
[2] M. Jiang, H.Y. Xiao, H.B. Zhang, S.M. Peng, C.H. Xu, Z.J. Liu, X.T. Zu, Acta Mater. 110 (2016) 192–199.
[3] H. Chen, H.M. Xiang, F.Z. Dai, J.C. Liu, Y.C. Zhou, J. Mater. Sci. Technol. 35 (2019) 2778–2784.
[4] Z.H. Zheng, J. Lv, M. Lou, K. Xu, L.L. Chen, J.B. Zhang, Y.J. Du, W.B. Zhang, K.K. Chang, Mater. Res. Lett. 11 (2022) 152–158.
[5] B. Deng, Z. Wang, W.Y. Chen, J.T. Li, D.X. Luong, R.A. Carter, G.H. Gao, B.I. Yakobson, Y.F. Zhao, J.M. Tour, Nat. Commun. 13 (2022) 262.
[6] B.C. Wyatt, S.K. Nemani, G.E. Hilmas, E.J. Opila, B. Anasori, Nat. Rev. Mater. 9 (2024) 773–789.
[7] X. Wang, J. Cortez, A.D. Dupuy, J.M. Schoenung, W.J. Bowman, Mater. Res. Lett. 11 (2022) 196–204.
[8] Y. Fan, J.F. Nie, Z.G. Ding, Y.J. Zhang, X. Chen, W. Liu, S. Yang, S.D. Liu, X.F. Liu, Y.H. Zhao, J. Mater. Sci. Technol. 204 (2025) 190–203.
[9] H.M. Xiang, Y. Xing, F.Z. Dai, H.J. Wang, L. Su, L. Miao, G.J. Zhang, Y.G. Wang, X.W. Qi, L. Yao, H.L. Wang, B. Zhao, J.Q. Li, Y.C. Zhou, J. Adv. Ceram. 10 (2021) 385–441.
[10] Z.C. Wang, S.Y. Chen, S.L. Yang, Q. Luo, Y.C. Jin, W. Xie, L.J. Zhang, Q. Li, J. Mater. Sci. Technol. 151 (2023) 41–65.
[11] J.F. Nie, Y.T. Zhi, Y. Fan, Y.H. Zhao, X.F. Liu, Mater. Res. Lett. 12 (2023) 88–96.
[12] P. Sarker, T. Harrington, C. Toher, C. Oses, M. Samiee, J.P. Maria, D.W. Brenner, K.S. Vecchio, S. Curtarolo, Nat. Commun. 9 (2018) 4980.
[13] Z.N. Cao, J.L. Sun, L.T. Meng, K.G. Zhang, J. Zhao, Z.F. Huang, X.L. Yun, J. Mater. Sci. Technol. 161 (2023) 10–43.
[14] C.A. Dennett, Z. Hua, E. Lang, F. Wang, B. Cui, Mater. Res. Lett. 10 (2022) 611–617.
[15] S.Y. Liu, S.X. Zhang, S.Y. Liu, D.J. Li, Y.P. Li, S.W. Wang, J. Eur. Ceram. Soc. 41 (2021) 6267–6274.
[16] S.Y. Liu, S.X. Zhang, S.Y. Liu, D.J. Li, Z.Q. Niu, Y.P. Li, S.W. Wang, J. Eur. Ceram. Soc. 42 (2022) 3089–3098.
[17] Y.C. Wang, M.J. Reece, Scr. Mater. 193 (2021) 86–90.
[18] K. Vecchio, S. Curtarolo, K. Kaufmann, T.J. Harrington, C. Oses, C. Toher, Acta Mater. 276 (2024) 120117.
[19] T.J. Harrington, J. Gild, P. Sarker, C. Toher, C.M. Rost, O.F. Dippo, C. Mcelfresh, K. Kaufmann, E. Marin, L. Borowski, P.E. Hopkins, J. Luo, S. Curtarolo, D.W. Brenner, K.S. Vecchio, Acta Mater. 166 (2019) 271–280.
[20] J.Y. Zhou, J.Y. Zhang, F. Zhang, B. Niu, L.W. Lei, W.M. Wang, Ceram. Int. 44 (2018) 22014–22018.
[21] W.L. Wang, G.X. Sun, X.N. Sun, Z.X. Zhang, J.T. Zhang, Y.J. Liang, J.Q. Bi, Mater. Res. Bull. 163 (2023) 112212.
[22] B.Y. Ye, S.S. Ning, D. Liu, T.Q. Wen, Y.H. Chu, J. Am. Ceram. Soc. 102 (2019) 6372–6378.
[23] L. Feng, W.G. Fahrenholtz, G.E. Hilmas, Y. Zhou, Scr. Mater. 162 (2019) 90–93.
[24] B.Q. Li, C. Liu, Z. Fang, Z.X. Yang, F. Ding, L.Y. Bai, C. Wang, F.L. Yuan, J. Eur. Ceram. Soc. 42 (2022) 6767–6773.
[25] B. Du, H.H. Liu, Y.H. Chu, J. Am. Ceram. Soc. 103 (2020) 4063–4068.
[26] S.S. Ning, T.Q. Wen, B.L. Ye, Y.H. Chu, J. Am. Ceram. Soc. 103 (2019) 2244–2251.
[27] F. Li, Y. Lu, X.G. Wang, W.C. Bao, J.X. Liu, F.F. Xu, G.J. Zhang, Ceram. Int. 45 (2019) 22437–22441.
[28] S.B. Jin, P. Shen, D.S. Zhou, Q.C. Jiang, Cryst. Growth Des. 12 (2012) 2814–2824.
[29] B.X. Dong, X.D. Ma, T.S. Liu, Q. Li, H.Y. Yang, S.L. Shu, B.Q. Zhang, F. Qiu, Q.C. Jiang, J. Am. Ceram. Soc. 104 (2021) 2820–2835.
[30] S.J. Hu, S.B. Li, W.M. Xu, W.B. Yu, Y. Zhou, Ceram. Int. 47 (2021) 29995–30004.
[31] M.G. Quesne, A. Roldan, N.H. De Leeuw, C.R.A. Catlow, Phys. Chem. Chem. Phys. 20 (2018) 6905–6916.
[32] D.Y. Wu, S.D. Ma, T. Jing, Y.D. Wang, L.S. Wang, J. Kang, Q. Wang, W. Wang, T. Li, R. Su, Acta Mater. 219 (2021) 117265.
[33] G. Wulff, Z. Kristallogr. 34 (1901) 449–530.
[34] J.M. Zhang, F. Ma, K.W. Xu, Appl. Surf. Sci. 229 (2004) 34–42.
[35] S.B. Jin, P. Shen, Q.L. Lin, L. Zhan, Q.C. Jiang, Cryst. Growth Des. 10 (2010) 1590–1597.
[36] R. Swaminathan, M.A. Willard, M.E. Mchenry, Acta Mater. 54 (2006) 807–816.
[37] B.X. Dong, F. Qiu, Q. Li, S.L. Shu, H.Y. Yang, Q.C. Jiang, Nanomaterials 9 (2019) 1152.
[38] G.D. Barmparis, Z. Lodziana, N. Lopez, I.N. Remediakis, Beilstein J. Nanotechnol. 6 (2015) 361–368.
[39] J.F. Nie, Y.Y. Wu, P.T. Li, H. Li, X.F. Liu, Cryst. Eng. Comm. 14 (2012) 2213–2221.
[40] A. Takeuchi, A. Inoue, Mater. Trans. 46 (2005) 2817–2829.
[41] J. Grammar, K. Ephesus, V. Hadjicontis, J. Phys. Chem. Solids 49 (1988) 1275–1277.
[42] H.Y. Luo, W.S. Liu, Y.Z. Ma, D.H. Xiao, C.P. Liang, J. Mater. Res. Technol. 30 (2024) 7104–7114.
[43] K.E. Knipling, D.C. Dunand, D.N. Seidman, Int. J. Mater. Res. 97 (2006) 246–265.
[44] G.Sai Gautam, K.C. Hari Kumar, J. Alloy. Compd. 587 (2014) 380–386.
[45] C. Bhattacharya, Comput. Mater. Sci. 127 (2017) 85–95.
[46] S. Jiang, L. Shao, T.W. Fan, J.M. Duan, X.T. Chen, B.Y. Ceram. Int. 46 (2020) 15104–15112.
[47] X. Geng, W.Z. Xu, X.X. Huang, C.Y. Ding, S.S. Wu, G.W. Wen, J. Am. Ceram. Soc. 105 (2022) 4942–4959.
[48] T.Q. Ren, R. Tran, S. Lee, A. Bandera, M. Herrera, X.G. Li, S.P. Ong, O.A. Graeve, J. Phys. Chem. C 125 (2021) 10665–10675.
[49] S. Zaima, Y. Shibata, H. Adachi, C. Oshima, S. Otani, M. Aono, Y. Ishizawa, Surf. Sci. 157 (1985) 380–392.
[50] Y.F. Liu, Y.X. Wei, R.F. Wu, Z.L. Fu, A.M. Chang, B. Zhang, J. Eur. Ceram. Soc. 44 (2024) 311–318.